Quantitative modeling of coupling-induced resonance frequency shift in microring resonators

Qing Li, Mohammad Soltani, Amir H. Atabaki, Siva Yegnanarayanan, and Ali Adibi

School of Electrical and Computer Engineering, Georgia Institute of Technology, 777 Atlantic Drive NW, Atlanta, GA 30332-0250
qli6@gatech.edu

Abstract: We present a detailed study on the behavior of coupling-induced resonance frequency shift (CIFS) in dielectric microring resonators. CIFS is related to the phase responses of the coupling region of the resonator coupling structure, which are examined for various geometries through rigorous numerical simulations. Based on the simulation results, a model for the phase responses of the coupling structure is presented and verified to agree with the simulation results well, in which the first-order coupled mode theory (CMT) is extended to second order, and the important contributions from the inevitable bent part of practical resonators are included. This model helps increase the understanding of the CIFS behavior and makes the calculation of CIFS for practical applications without full numerical simulations possible.

OCIS codes: (130.3120) Integrated optics devices; (230.5750) Resonators

References and links

1. G. T. Reed, and A. P. Knights, *Silicon Photonics: An Introduction*, (John Wiley, West Sussex, 2004).
2. L. Pavesi, and D. J. Lockwood, *Silicon Photonics*, (Springer-Verlag, New York, 2004).
3. K. Vahala, *Optical Microcavities*, (World Scientific, Singapore, 2004).
4. B. E. Little, S. T. Chu, H. A. Haus, J. Foresi, and J.-P. Laine, "Microring resonator channel dropping filters," J. Lightwave Technol. **15**(6), 998–1005 (1997).
5. F. Xia, M. Rooks, L. Sekaric, and Y. Vlasov, "Ultra-compact high order ring resonator filters using submicron silicon photonic wires for on-chip optical interconnects," Opt. Express **15**(19), 11934–11941 (2007).
6. F. Xia, L. Sekaric, and Y. Vlasov, "Ultracompact optical buffers on a silicon chip," Nat. Photonics **1**(1), 65–71 (2007).
7. B. Liu, A. Shakouri, and J. E. Bowers, "Passive microring-resonator-coupled lasers," Appl. Phys. Lett. **79**(22), 3561–3563 (2001).
8. K. De Vos, I. Bartolozzi, E. Schacht, P. Bienstman, and R. Baets, "Silicon-on-Insulator microring resonator for sensitive and label-free biosensing," Opt. Express **15**(12), 7610–7615 (2007).
9. M. A. Popovic, C. Manolatou, and M. R. Watts, "Coupling-induced resonance frequency shifts in coupled dielectric multi-cavity filters," Opt. Express **14**(3), 1208–1222 (2006).
10. Q. Li, S. Yegnanarayanan, A. Atabaki, and A. Adibi, "Calculation and correction of coupling-induced resonance frequency shifts in traveling-wave dielectric resonators," in Integrated Photonics and Nanophotonics Research and Applications, (Optical Society of America, 2008), paper IWH3. *http://www.opticsinfobase.org/abstract.cfm?URI=IPNRA-2008-IWH3*
11. Q. Li, M. Soltani, S. Yegnanarayanan, and A. Adibi, "Design and demonstration of compact, wide bandwidth coupled-resonator filters on a siliconon- insulator platform," Opt. Express **17**(4), 2247–2254 (2009).
12. Y. Tsuji, and M. Koshiba, "Finite element method using port truncation by perfectly matched layer boundary conditions for optical waveguide discontinuity problems," J. Lightwave Technol. **20**(3), 463–468 (2002).
13. H. A. Haus, *Waves and fields in optoelectronics* (Prentice-Hall, Englewood Cliffs, NJ, 1984).
14. A. Hardy, and W. Streifer, "Coupled mode theory of parallel waveguides," J. Lightwave Technol. **3**(5), 1135–1146 (1985).
15. S. L. Chuang, "A coupled mode formulation by reciprocity and a variational principle," J. Lightwave Technol. **5**(1), 5–15 (1987).
16. D. Marcuse, *Theory of Dielectric Optical Waveguides*, second edition (Academic, Boston, 1991), Chap. 6.
17. D. Khalil, "On the radiation mode effects in integrated optical directional couplers," Opt. Quantum Electron. **31**(2), 151–159 (1999).
18. A. Melloni, F. Carniel, R. Costa, and M. Martinelli, "Determination of bend mode characteristics in dielectric waveguides," J. Lightwave Technol. **19**(4), 571–577 (2001).

#118220 - $15.00 USD Received 6 Oct 2009; revised 29 Nov 2009; accepted 30 Nov 2009; published 7 Dec 2009

19. For example, for the material system used in Ref. [9], $\Delta\beta$ is numerically found to be negative and small (~-0.015 μm^{-1} at 1578nm for TE polarization, w_1/w_2 = 400/400 nm, and *gap* = 100 nm). The corresponding simulation results are shown in Fig. 6 in Ref. [9]. We already know $\Delta\psi$ is negative for this coupling geometry ("CB" coupler), and therefore both terms in Eqs. (23) are negative and the second term is dominant. The two features that ϕ_{11} (ring-ring phase) is negative (corresponding CIFS positive) and ϕ_{11} and ϕ_{22} are of opposite signs are readily understood from Eqs. (23) and (24).
20. M. Soltani, *Novel integrated silicon nanophotonic structures using ultra-high Q resonator*, Ph.D. dissertation, Georgia Institute of Technology (2009)
21. M. Popovic, "Complex-frequency leaky mode computations using PML boundary layers for dielectric resonant structures," in Proceedings of Integrated Photonics Research (Washington, DC, June 17, 2003).

1. Introduction

Dielectric microring resonators are key microphotonic circuit components [1–3], and several recent works have utilized them in both single-resonator and coupled-resonator architectures for realizing complex functionalities in a planar platform for applications like bandpass filters [4,5], slow-wave structures [6], on-chip lasers [7], and sensing elements [8]. In coupled-resonator structures, where the response is engineered by appropriate choice of the resonance frequencies of each single resonator and their mutual coupling strengths, one critical issue is the precise control of the resonance frequency, which depends on both the resonator material and the resonator structure. In addition, it has been shown that when it is coupled to access waveguides or adjacent resonators, the resonance frequency of a resonator will deviate from its original isolated value [9,13]. Such coupling-induced resonance frequency shift (CIFS), which is recently investigated more systematically [9], causes resonance frequency mismatches between individual resonators and thus significantly impacts the performance of the coupled-resonator device [9–11].

The work in Ref [9]. gives an excellent explanation on the origin of CIFS, especially, that CIFS is beyond the first-order coupled mode theory (CMT) and sometimes could be counterintuitive. Two interesting features of CIFS shown by Ref [9]. are: 1) despite the expectation of a negative CIFS from positive-index perturbations, CIFS can be of positive or negative sign, i.e., the resonance frequency of a resonator can be either blue shifted or red shifted by the coupling effect; and 2) two coupled microrings with different radii can experience CIFS of opposite signs, one being positive and the other being negative. However, Ref [9]. focuses on the qualitative discussions of the second-order, self-perturbing frequency shift term in the CMT formalism, and it concludes that quantitative calculation using the first-order CMT is not exact due to the existence of inevitable errors. As a result, currently CIFS calculation must be performed using laborious numerical simulations, where little physical insight is gained. In fact, the understanding of CIFS is so limited that for a given material system and resonator coupling structure, the estimation of the sign or the order of magnitude of CIFS is still difficult.

In this work, we present a detailed investigation of CIFS for dielectric microring resonators. As observed in Refs [9,10], we show that CIFS can be related to the phase responses of the coupling region in the resonator coupling structure. Due to this relationship, CIFS study is facilitated by developing a more accurate analysis tool for the coupling structures beyond the first-order CMT. To do this, we first simulate resonator coupling structures with efficient numerical simulations to obtain the phase responses for structures with different geometric properties. Subsequently a model is developed to help understand the simulation results, in which the CMT is naturally extended to second order. In addition, geometric effects are included, among which the effect of the inevitable bent part of practical resonators is revealed as an important contributor to the final phase responses. This model is then verified to agree with the simulation results by quantitative examinations, and finally a conclusion is given.

2. CIFS in microring resonators

For microring resonators coupled to access waveguides or adjacent resonators, the coupling region can be treated as a multi-port coupler. Figure 1 shows two such examples with different coupling geometries. Here a_1, b_1 stand for the input and output signals travelling inside the

#118220 - $15.00 USD Received 6 Oct 2009; revised 29 Nov 2009; accepted 30 Nov 2009; published 7 Dec 2009

resonator under investigation, respectively, and a_2, b_2 stand for the input and output signals travelling inside the access waveguide or the adjacent resonator, respectively. To facilitate the CIFS simulation, waveguides and resonators are terminated beyond the coupling region by perfectly matched layers (PMLs), and the signal source is also implemented [12], as will be discussed later. We also assume that the reference planes for a_i and b_i (i = 1, 2) are far from the coupling region, and the signals are normalized in a way that $|a_i|^2$ and $|b_i|^2$ (i = 1, 2) represent powers at each port. If the coupling is lossless and reflection is negligible, the output signals can be related to the input signals by a unitary 2 × 2 transfer matrix as [9],

$$\begin{bmatrix} b_1 \\ b_2 \end{bmatrix} = U \begin{bmatrix} a_1 \\ a_2 \end{bmatrix} = \begin{bmatrix} u_{11}e^{i\phi_{11}} & u_{12}e^{i\phi_{12}} \\ u_{21}e^{i\phi_{21}} & u_{22}e^{i\phi_{22}} \end{bmatrix} \begin{bmatrix} a_1 \\ a_2 \end{bmatrix} \tag{1}$$

where u_{ij}, ϕ_{ij} (i, j = 1, 2) are the amplitude and phase responses of each component of the transfer matrix U, respectively. As a convention, in Eq. (1) we have assumed that the free propagation phase term, namely, the phase contribution resulting from wave propagation from the reference plane of a_1 (a_2) to that of b_1 (b_2) in the absence of coupling is excluded. In this sense, phase responses ϕ_{11}, ϕ_{22} result from pure coupling interaction and will asymptotically approach zero when the coupling is weakened to a negligible extent.

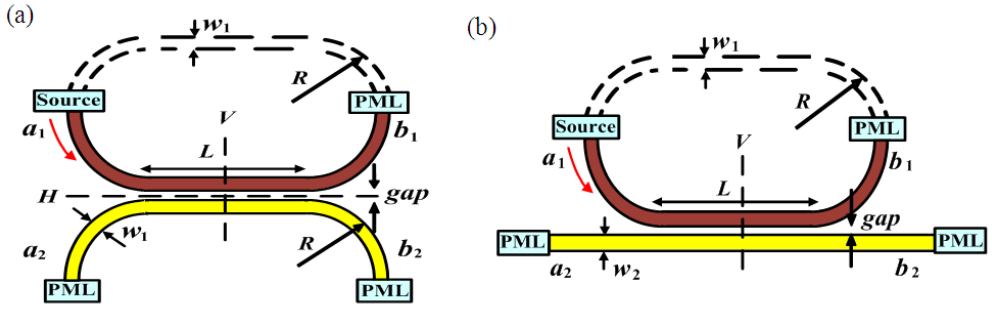

Fig. 1. Two typical coupler architectures with different coupling geometries. a_1, a_2 are the input signals and b_1, b_2 are the corresponding output signals; L is the length of the middle straight part; R is the outer bend radius; *gap* is the spacing between edges of the two waveguides, and w_1, w_2 are the waveguide widths as shown. The brown region is the waveguide core at the resonator side, and the yellow region, which shows the access waveguide or part of the adjacent resonator, can be changed to be either waveguide core or cladding to obtain the net phase shift from the coupling effect. (a) Coupler CA with vertical symmetry axis V and horizontal symmetry axis H. (b) Coupler CB with vertical symmetry axis V.

The effect of coupling on the resonance frequency of the resonator is then modeled as the added phase to the signal travelling inside the resonator as it passes through the coupling region, which is ϕ_{11} as we have defined. Using the fact that a round-trip net phase shift of 2π will shift the resonance frequency by one free spectral range (FSR), CIFS can be approximated as [9,10],

$$CIFS \approx -\frac{\phi_{11}}{2\pi}\Delta f_{FSR} = -\frac{\phi_{11}}{2\pi}\frac{c}{n_g S} \tag{2}$$

where Δf_{FSR} is the FSR, c is the speed of light in vacuum, n_{g} is the group index at the resonance frequency, and S is the perimeter of the resonator. The negative sign in Eq. (2) is due to the convention used throughout this paper for the propagation phase term as $\exp(i\beta z)$ with β being the propagation constant and z being the coordinate in the direction of propagation. Because of Eq. (2), calculation of CIFS is equivalent to the calculation of the phase term ϕ_{11}. In addition, if a_2 and b_2 represent the travelling signals inside an adjacent coupled resonator, CIFS of that adjacent resonator will be given by a similar expression as Eq.

#118220 - $15.00 USD Received 6 Oct 2009; revised 29 Nov 2009; accepted 30 Nov 2009; published 7 Dec 2009

(2), with phase term ϕ_{11} replaced by ϕ_{22}. Therefore, in the rest of the paper, we will focus on the study of the phase responses of the coupling region instead of direct CIFS calculations. Once we have a thorough understanding of the phase behaviors of the transfer matrix *U*, CIFS calculation using Eq. (2) is straightforward (see Appendix A for more discussions).

Before going into detailed calculation of these phase terms, it is worthwhile to mention some general properties of the transfer matrix *U* imposed by power conservation and symmetry considerations. Power conservation requires *U* to be unitary, and this imposes that *U* can be written as [9],

$$U = \begin{bmatrix} u_{11}e^{i\phi_{11}} & u_{12}e^{i\phi_{12}} \\ u_{21}e^{i\phi_{21}} & u_{22}e^{i\phi_{22}} \end{bmatrix} = e^{i\theta_0}\begin{bmatrix} \sqrt{1-\kappa^2}\,e^{i\theta_1} & i\kappa e^{i\theta_2} \\ i\kappa e^{-i\theta_2} & \sqrt{1-\kappa^2}\,e^{-i\theta_1} \end{bmatrix} \tag{3}$$

where θ_0, θ_1, θ_2 are phase parameters related to ϕ_{ij} (i, j = 1, 2), and κ is the magnitude of the field coupling coefficient between the two coupled structures shown in Fig. 1 (κ^2 is the power coupling coefficient). From Eq. (3), it is easy to observe that

$$u_{12} = u_{21} = \kappa \tag{4}$$

$$\phi_{11} + \phi_{22} = \phi_{12} + \phi_{21} - \pi \tag{5}$$

When the couplers have the symmetry about the middle vertical axis (i.e., axis *V* shown in Fig. 1), reciprocity and symmetry considerations give [9,10]

$$\frac{\phi_{11} + \phi_{22}}{2} = \phi_{12} - \frac{\pi}{2} = \phi_{21} - \frac{\pi}{2} \tag{6}$$

Moreover, if the coupler has the additional symmetry about the middle horizontal axis in the coupling region, as shown by axis *H* in Fig. 1(a), symmetry requires that [10]

$$\phi_{11} = \phi_{22} = \phi_{12} - \frac{\pi}{2} = \phi_{21} - \frac{\pi}{2} \tag{7}$$

Note that for the coupler shown in Fig. 1(b) no such horizontal axis exists, and hence, in general $\phi_{11} \neq \phi_{22}$.

To explore the phase properties of the transfer matrix *U*, we carry out a detailed analysis for the two typical coupling structures shown in Fig. 1. Waveguides are terminated and resonators are broken to implement the signal source and PMLs. The resulting couplers, named CA and CB, respectively, are then analyzed with the finite element method (details in Appendix A). The first coupler CA shown in Fig. 1(a) has two symmetry axes, the vertical axis *V* and the horizontal axis *H*. As a result, the phase terms have the properties given by Eq. (7). The second coupler CB shown in Fig. 1(b) only has the vertical symmetry axis *V*, and its phase properties are given by Eq. (6). Simulations for these two couplers are performed at a fixed frequency and for varying coupling parameters (e.g., the length of the middle straight part *L* and the waveguide widths w_1, w_2 as shown in Fig. 1). The phase term ϕ_{11} (ϕ_{21}) can be obtained by comparing the phase difference of b_1 (b_2) with and without the presence of the coupling waveguide (shown by the yellow region in Fig. 1) with the source implemented at the a_1 side, as the case shown in Fig. 1. Similarly, the phase terms ϕ_{22} and ϕ_{12} can be obtained with the source implemented at the a_2 side.

3. Simulation results and discussions

We choose the silicon-on-insulator (SOI) material system in our simulations, and we simulate the fundamental TE-like polarization (electric field predominantly in the plane of the structure). Using the effective index method to simplify the 3-dimensional (3-D) structures to 2-dimensional (2-D), one obtain an effective index of 2.829 for the silicon layer at wavelength

#118220 - $15.00 USD Received 6 Oct 2009; revised 29 Nov 2009; accepted 30 Nov 2009; published 7 Dec 2009

1578nm, assuming a silicon thickness of 220 nm on top of a thick enough (at least 1μm) buried oxide (BOX) layer and an air cladding.

3.1 Simulations: couplers with identical waveguide widths

We first simulate couplers with identical waveguide widths, i.e., $w_1 = w_2$ as in Fig. 1. Phase responses are obtained for various straight part lengths L, with the bend radius R and the gap between waveguides fixed at 6 μm and 100 nm, respectively. Moreover, the power coupling coefficient κ^2 (defined in Eq. (3)), which reflects the magnitude of coupling strength, is also obtained. Figure 2 shows the simulation results (shown by marker) for the coupler CA with the simulation parameters listed in Fig. 2(a), while Fig. 3 shows the simulation results for the coupler CB in a similar way. In addition, we have plotted the modeling results (shown by dotted line) for both couplers (the details of the model will be discussed in the next subsection).

(a)

coupler	CA
$n_{WG}/n_{Cladding}$	2.829/1
w_1/w_2 (nm)	400/400
gap (nm)	100
wavelength (nm)	1578

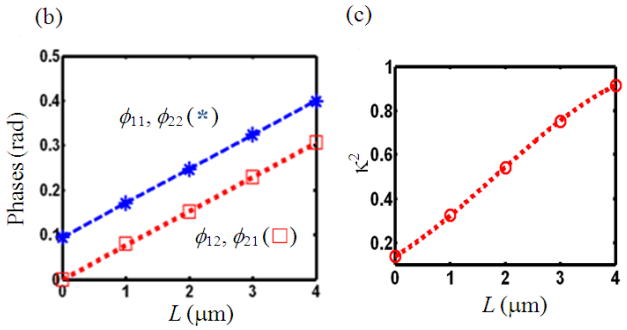

Fig. 2. (a) Simulation parameters for the coupler CA shown in Fig. 1(a). The bend radius R is 6 μm; the waveguide width w_1 is 400 nm, and the *gap* is 100 nm. n_{WG} and $n_{Cladding}$ are the refractive indices of the waveguide core and cladding, respectively, as obtained from the effective index method. Simulation (marker) and modeling (dotted line) results of the coupler CA as a function of the straight part length L are shown for (b) phase responses (for the sake of clarity, ϕ_{12} (ϕ_{21}) is plotted relative to its value at $L = 0$), and (c) power coupling coefficient κ^2.

(a)

coupler	CB
$n_{WG}/n_{Cladding}$	2.829/1
w_1/w_2 (nm)	400/400
gap (nm)	100
wavelength (nm)	1578

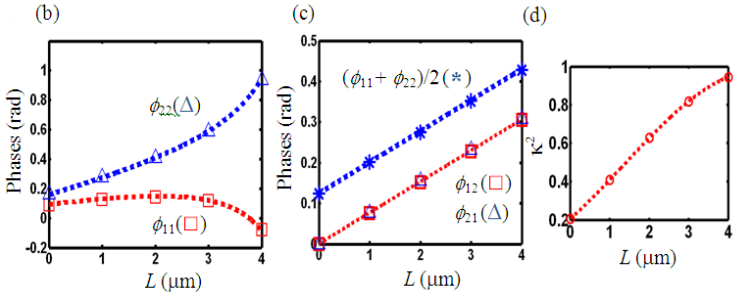

Fig. 3. (a) Simulation parameters for the coupler CB shown in Fig. 1(b). The bend radius R is 6 μm; the waveguide widths w_1 and w_2 are both 400 nm, and the *gap* is 100 nm. Simulation (marker) and modeling (dotted line) results of the coupler CB as a function of the straight part length L are shown for (b) phase responses ϕ_{11}, ϕ_{22}, (c) phase responses ϕ_{12} ,ϕ_{21}, and (ϕ_{11} + ϕ_{22})/2 (for the sake of clarity, ϕ_{12} (ϕ_{21}) is plotted relative to its value at $L = 0$), and (d) power coupling coefficient κ^2.

From Fig. 2(b), we observe that for the coupler CA: 1) the requirements from power conservation and symmetry considerations given by Eq. (7) are satisfied; 2) the phase terms ϕ_{11} (ϕ_{22}), ϕ_{12} (ϕ_{21}) are linear with L with the same slope. From Fig. 3, we observe that for the coupler CB: 1) the requirements from power conservation and symmetry considerations given by Eq. (6) are satisfied, as shown by Fig. 3(c); 2) $\phi_{11} \neq \phi_{22}$, and both are nonlinear with L, as shown by Fig. 3(b). It is especially interesting to note that, ϕ_{11} is positive at $L = 0$ and slightly

#118220 - $15.00 USD Received 6 Oct 2009; revised 29 Nov 2009; accepted 30 Nov 2009; published 7 Dec 2009

increases for small values of L. When L is large enough, the coupling becomes strong, and ϕ_{11} starts to decrease with L, eventually to a negative value. That means the corresponding CIFS, as easily seen from Eq. (2), is negative when L is small and becomes positive when L is large enough. In contrast, for the coupler CA, CIFS is always negative and doesn't change sign as L increases; 3) ϕ_{12}, ϕ_{21} and $(\phi_{11} + \phi_{22})/2$ are linear with L with the same slope, and this slope is the same as that shown in Fig. 2(b).

3.2 Modeling of transfer matrix U

To understand the simulation results presented in the previous subsection 3.1, we analyze the coupler structures shown in Fig. 1 in more detail in this subsection. Both the couplers CA and CB are composed of three parts: input bend, middle straight part, and output bend, as shown in Fig. 4. Each component can be described by a transfer matrix. For example, the transfer matrix B for the input bend relates $[c_1, c_2]^T$ to $[a_1, a_2]^T$ while the transfer matrix T for the middle straight part relates $[d_1, d_2]^T$ to $[c_1, c_2]^T$. Here $[c_1, c_2]^T$ and $[d_1, d_2]^T$ are the input and output optical signals for the middle straight part. Power conservation requires that both matrices B and T to be unitary. In addition, because of the symmetry about the vertical axis and the reciprocity, the transfer matrix for the output bend can be shown to be B^T, which relates $[b_1, b_2]^T$ to $[d_1, d_2]^T$. The total transfer matrix U, as a result, is given by [10]

$$U = NB^T TB \tag{8}$$

where N is a normalization matrix to remove the free propagation phase contribution because of the convention made in defining the transfer matrix U in Eq. (1).

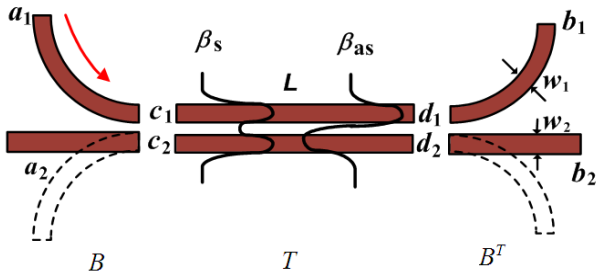

Fig. 4. Three components comprising the coupler CA (lower part of input and output bends by dashed line) and CB (lower part of input and output bends by solid line) originally defined in Fig. 1: input bend, middle straight part, and output bend, which are modeled by transfer matrices B, T and B^T, respectively. The two fundamental system modes of the middle parallel waveguide coupler are schematically shown on the middle part of the coupler.

The middle straight part is a parallel waveguide coupler and has been extensively studied using the CMT [13–15]. In principle, this coupled system can be exactly analyzed by expanding the individual waveguide modes by the complete set of system modes (or supermodes) [13]. If the waveguides are single mode, and the gap between them is not too small, limiting the expansion to the lowest two fundamental system modes usually suffices [14,15]. For the particular case of $w_1 = w_2$, the field profiles of the two fundamental system modes, i.e., the symmetric mode and the antisymmetric mode, with different propagation constants β_s and β_{as}, respectively, are schematically shown in Fig. 4. Although in the case $w_1 \neq w_2$, the two system modes do not have simple symmetry relating to the individual waveguide modes, we shall still use β_s and β_{as} to denote the propagation constants for these two system modes. In this paper, we will focus on the cases that the two waveguides are either exactly or close to be phase matched. As a result, the transfer matrix T for the middle parallel waveguide coupler can be expressed as [16],

#118220 - $15.00 USD Received 6 Oct 2009; revised 29 Nov 2009; accepted 30 Nov 2009; published 7 Dec 2009

$$T = e^{i(\frac{\beta_s+\beta_{as}}{2})L}\begin{bmatrix} \cos(\beta_0 L)+i\frac{\delta}{\beta_0}\sin(\beta_0 L) & i\frac{\bar{\kappa}}{\beta_0}\sin(\beta_0 L) \\ i\frac{\bar{\kappa}}{\beta_0}\sin(\beta_0 L) & \cos(\beta_0 L)-i\frac{\delta}{\beta_0}\sin(\beta_0 L) \end{bmatrix} \quad (9)$$

where δ is the phase mismatch between the two waveguides defined as $\delta \equiv (\beta_1 - \beta_2)/2$, with β_1, β_2 corresponding to the propagation constants of individual waveguides with widths w_1, w_2 respectively; $\bar{\kappa}$ is the field coupling coefficient between two waveguides, and

$$\beta_0 \equiv \frac{\beta_s - \beta_{as}}{2} = \sqrt{\bar{\kappa}^2 + \delta^2} \quad (10)$$

We have to point out that though Eq. (9) has a similar form as the one obtained from CMT, they are different. In CMT, $\bar{\kappa}$ is obtained from the field overlap of individual waveguide modes, and β_0 is obtained from the knowledge of $\bar{\kappa}$ and δ [9,13]. In the system modes approach outlined here, β_s and β_{as} are numerically calculated with desired accuracy, and β_0 is obtained via Eq. (10), in which $\bar{\kappa}$ can also be obtained from the knowledge of β_0 and δ. Since β_s and β_{as} can be calculated accurately from numerical simulations, the system modes approach is in general more accurate than the CMT approach.

If $w_1 = w_2$, the parallel waveguide coupler is synchronous and hence $\delta = 0$ ($\beta_1 = \beta_2$) and $\beta_0 = \bar{\kappa}$ (Eq. (10)). In this case, Eq. (9) can be simplified as

$$T = e^{i\beta_1 L}e^{i\Delta\beta L}\begin{bmatrix} \cos(\beta_0 L) & i\sin(\beta_0 L) \\ i\sin(\beta_0 L) & \cos(\beta_0 L) \end{bmatrix} \quad (11)$$

where $\Delta\beta \equiv (\beta_s + \beta_{as} - \beta_1 - \beta_2)/2$. Equation (11) shows that besides the free propagation phase contribution $\exp(i\beta_1 L)$, additional phase term $\exp(i\Delta\beta L)$ appears. By combining the definitions of β_0 and $\Delta\beta$, we can rewrite β_s and β_{as} as

$$\beta_s = \beta_1 + \beta_0 + \Delta\beta \quad (12)$$

$$\beta_{as} = \beta_1 - \beta_0 + \Delta\beta \quad (13)$$

Equations (12) and (13) can be regarded as Taylor expansions of the propagation constants of the coupled system modes as a function of coupling coefficients. When the two identical waveguides are well separated (i.e., $\beta_0 \approx 0$), the system has two degenerate modes with propagation constants $\beta_1 = \beta_2$. As the two waveguides are brought closer, the degeneracy is removed, and the new propagation constants β_s and β_{as} can be expanded based on the different orders of the coupling perturbation. In Eqs. (12) and (13), we actually expand the propagation constants of the two fundamental system modes up to the second order of the coupling perturbation, while in CMT the expansion is only up to the first order. The linear phase behavior with L observed in Figs. 2(b) and 3(c) can be identified with this second-order phase term $\exp(i\Delta\beta L)$, with the slope $\Delta\beta$ provided in Table 1 for the middle parallel waveguide coupler simulated in Figs. 2 and 3.

However, we observe that the CA and CB couplers show different results, as seen in Figs. 2 and 3. For the coupler CA, the phase responses shown in Fig. 2(b) are all linear with L, which is similar to that given by Eq. (11) for the synchronous parallel waveguide coupler except a constant difference. For the coupler CB, the phase responses shown in Figs. 3(b) and 3(c) illustrate some similarities with a synchronous parallel waveguide coupler, and also some significant differences, especially for the phase terms ϕ_{11} and ϕ_{22}. This suggests that the bent parts are important to the final phase responses, and the corresponding transfer matrix B has to be included in the model.

Since the transfer matrix B relating $[c_1, c_2]^T$ to $[a_1, a_2]^T$ as shown in Fig. 4 is assumed to be unitary, it has a similar expression as Eq. (3) and is expressed by

#118220 - $15.00 USD Received 6 Oct 2009; revised 29 Nov 2009; accepted 30 Nov 2009; published 7 Dec 2009

$$B = e^{i\alpha_0} e^{i\Delta\beta z_p} \begin{bmatrix} \cos(\beta_0 z_a) e^{i\Delta\psi} & i\sin(\beta_0 z_a) \\ i\sin(\beta_0 z_a) & \cos(\beta_0 z_a) e^{-i\Delta\psi} \end{bmatrix} \tag{14}$$

In writing Eq. (14), we model the bent part by the middle parallel waveguide coupler along with some modifications, with parameters $\{\beta_0, \Delta\beta\}$ correspond to those of the middle parallel waveguide coupler with the specified gap. Unlike in Eq. (11) where the only length parameter is the physical length L, z_p and z_a are introduced as equivalent lengths to lump the phase and amplitude responses of the bent part, respectively [17]. The reference planes of $[a_1, a_2]^T$ are chosen such that the phase difference between c_1 and a_2 is equal to that between c_2 and a_1, which is reflected by the fact that the off-diagonal elements of transfer matrix B are equal in Eq. (14) (Appendix B). With this choice of the reference planes of $[a_1, a_2]^T$, generally the phase difference between c_1 and a_1 is not equal to that between c_2 and a_2, and $\Delta\psi$ is introduced to account for this difference. α_0 is a constant and its meaning can be better understood in the following paragraph.

The normalization matrix N can be calculated based on its definition, i.e., to remove the free propagation phase contributions in the absence of coupling. In this sense, N has two diagonal elements, each corresponding to the phase difference between a_i (i = 1, 2) and b_i (i = 1, 2) when the coupling effect is negligible. Because of the nature of free propagation, the phase contributions from different components in Fig. 4 can be added to obtain the overall propagation phases. For the middle parallel waveguide coupler, the calculation is straightforward: $\exp(i\beta_1 L)$ for the upper waveguide, and $\exp(i\beta_2 L)$ for the lower waveguide. For the input bend, it is a little complicated. Based on the definition of the transfer matrix B (Eq. (14)), the free propagation phases can be approximated as $\exp(i(\alpha_0 + \Delta\psi))$ for the upper arm, and $\exp(i(\alpha_0 - \Delta\psi))$ for the lower arm, respectively (we put the details in the Appendix B). For the output bend, the transfer matrix is B^T, and the free propagation phases will be the same as those of the input bend. Finally, we obtain N as,

$$N = \begin{bmatrix} e^{-i[2(\alpha_0 + \Delta\psi) + \beta_1 L]} & 0 \\ 0 & e^{-i[2(\alpha_0 - \Delta\psi) + \beta_2 L]} \end{bmatrix} \tag{15}$$

The transfer matrix U can thus be obtained from Eq. (8), with matrices T, B, and N given by Eqs. (9), (14), and (15), respectively. The parameters $\{\bar{\kappa}, \delta, \beta_0, \Delta\beta\}$ are numerically obtained from the middle parallel waveguide coupler by solving the coupler's lowest two fundamental system modes, and the unknowns $\{\Delta\psi, z_p, z_a\}$ are fitted based on the simulation results of the transfer matrix U.

3.3 Modeling results: couplers with identical waveguide widths

For couplers with identical waveguide widths $w_1 = w_2$, simulation and modeling results are shown in Figs. 2 and 3 for the couplers CA and CB, respectively, where good agreement is observed. The corresponding modeling parameters and fitting results are provided in Table 1.

For the coupler CA $\Delta\psi = 0$ due to the symmetry about the horizontal axis. After a straightforward calculation for the transfer matrix U, we obtain,

$$\phi_{11} = \phi_{22} = \phi_{12} - \frac{\pi}{2} = \phi_{21} - \frac{\pi}{2} = \Delta\beta(L + 2z_p) \tag{16}$$

$$\kappa^2 = \sin^2(\beta_0(L + 2z_a)) \tag{17}$$

which show that the net effect of the input and output bends of the coupler CA is equal to a parallel waveguide coupler with the same gap as the middle straight part, but with effective lengths of $2z_p$ and $2z_a$ for the phase and amplitude responses, respectively. This is exactly what we observe from Fig. 2.

#118220 - $15.00 USD Received 6 Oct 2009; revised 29 Nov 2009; accepted 30 Nov 2009; published 7 Dec 2009

Table 1. Modeling parameters and fitting results for the coupled structures shown in Figs. 2, 3 and 6

Figures		$\bar{\kappa}$ (μm^{-1})	δ(μm^{-1})	$\Delta\beta$(μm^{-1})	$\Delta\psi$(rad)	z_p(μm)	z_a(μm)
Fig. 2		0.224	0	0.077	0	0.618	0.849
Fig. 3		0.224	0	0.077	−0.261	0.811	1.095
Fig.6	w_2 = 390nm	0.234	0.069	0.08	−0.22	0.81	1.095
	w_2 = 410nm	0.211	−0.064	0.073	−0.285	0.819	1.025

For the coupler CB $\Delta\psi\neq 0$, and the results are more complicated. For small $|\Delta\psi|$ (<0.5 rad), $\exp(i\Delta\psi)\approx 1 + i\Delta\psi$ in Eq. (14), and we obtain for small $|\phi_{11}|$ and $|\phi_{22}|$ (<0.5 rad) after a simple though tedious computation for the transfer matrix U,

$$\phi_{12} - \frac{\pi}{2} = \phi_{21} - \frac{\pi}{2} = \Delta\beta(L + 2z_p) \tag{18}$$

$$\phi_{11} \approx \Delta\beta(L + 2z_p) + 2\Delta\psi \sin(\beta_0 z_a) \frac{\sin(\beta_0 (L + z_a))}{\cos(\beta_0 (L + 2z_a))} \tag{19}$$

$$\phi_{22} \approx \Delta\beta(L + 2z_p) - 2\Delta\psi \sin(\beta_0 z_a) \frac{\sin(\beta_0 (L + z_a))}{\cos(\beta_0 (L + 2z_a))} \tag{20}$$

Equations (18)-(20) can be used to explain the simulation results shown in Fig. 3. The first observation is that ϕ_{12}, ϕ_{21}, and $(\phi_{11} + \phi_{22})/2$ are linear with L with a slope of $\Delta\beta$. Since $\Delta\beta$ is defined for the middle straight part which is shared by CA and CB with the same parameters in Figs. 2 and 3, it is expected and verified that the slope observed in Fig. 2(b) is equal to that observed in Fig. 3(c). Moreover, both ϕ_{11} and ϕ_{22} have two terms, one is linear with L and the other is nonlinear with L. It is clear that the magnitude of the second term in Eqs. (19)-(20) is small at small values of L, but at large L, this term starts to dominate the first term. Thus, we expect ϕ_{11} and ϕ_{22} to vary linearly with L only for small L. At large L, we expect ϕ_{11} to increase (if $\Delta\psi$ is positive) or decrease (if $\Delta\psi$ is negative) nonlinearly with L. Results shown in Figs. 3(b) and 3(c) indicate that $\Delta\beta$ is positive and $\Delta\psi$ is negative, since ϕ_{11} eventually decreases to a negative value. On the contrary, in ϕ_{22} both terms are of positive sign, therefore it increases with L monotonically as shown in Fig. 3(b).

The negative sign of $\Delta\psi$ is believed to be intrinsic to the geometry of the coupler CB, which has been explained using the geometry conformal mapping argument in Ref [10]. For the upper bend, the propagation constant of the travelling signal is roughly equal to that of a straight waveguide with the same width when the bend radius is not too small [18]. In writing Eq. (14), we have chosen the reference planes of $[a_1, a_2]^T$ such that the off-diagonal elements of the transfer matrix B are equal. It seems that with this choice of reference planes, the propagation path from the reference plane of a_1 to that of c_1 is shorter than the propagation path from the reference plane of a_2 to that of c_2, resulting a negative $\Delta\psi$ when $w_1 = w_2$ (from Eq. (14) $\exp(i2\Delta\psi)$ is the phase difference between the upper and the lower arms). This explanation could be qualitatively understood from Fig. 5(a).

Based on this understanding, the variations of $\Delta\psi$ for the coupler CB with the geometric parameters can be predicted. For example, we fix the upper waveguide width w_1 and change the lower waveguide width w_2. When w_2 is larger than w_1, the propagation constant of the lower arm (a_2 to c_2) is larger than that of the upper arm (a_1 to c_1). Also, we already know that propagation length of the lower arm (a_2 to c_2) is larger than that of the upper arm (a_1 to c_1). As a result, $\Delta\psi$ will be smaller and more negative than that in the $w_1 = w_2$ case. On the contrary, if w_2 is less than w_1, the propagation constant of the lower arm (a_2 to c_2) is smaller than that of the upper arm (a_1 to c_1). Thus, $\Delta\psi$ will be larger than that in the $w_1 = w_2$ case. If we keep reducing w_2, $\Delta\psi$ will increase from a negative value to an eventual positive value. This

#118220 - $15.00 USD Received 6 Oct 2009; revised 29 Nov 2009; accepted 30 Nov 2009; published 7 Dec 2009

behavior of $\Delta\psi$ is schematically shown in Fig. 5(b), and we will investigate these predicted properties in the following subsections.

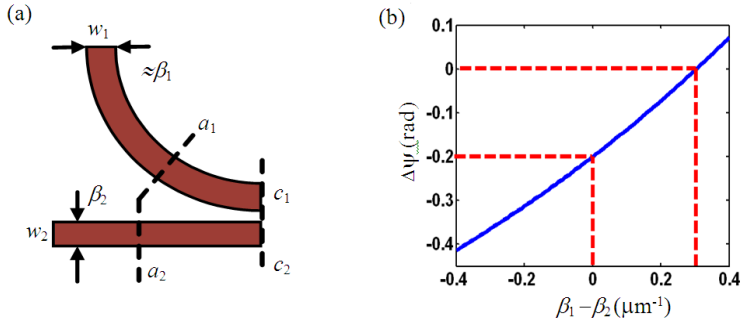

Fig. 5. (a) Input bend of the coupler CB shown in Fig. 1(b), which consists of the upper bent waveguide with width w_1 and the lower straight waveguide with width w_2. β_1, β_2 are the propagation constants of individual straight waveguides with widths w_1 and w_2, respectively. The reference planes of $[a_1, a_2]^T$ and $[c_1, c_2]^T$ are shown by the dashed line. From the simulation and modeling results of Fig. 3 we conclude that the length of propagation path from a_1 to c_1 is smaller than that from a_2 to c_2, resulting a negative $\Delta\psi$ when $\beta_1 = \beta_2$. (b) A schematic drawing $\Delta\psi$ of as a function of $(\beta_1-\beta_2)$. The numbers are just shown for illustrative purpose and not exact.

3.4 Modeling results: couplers with different waveguide widths

To verify our model and also explore the properties of $\Delta\psi$, we proceed to survey more examples by simulating the coupler CB with different waveguide widths, i.e., $w_1 \neq w_2$, and performing the modeling accordingly. For small $|\Delta\psi|$ (<0.5 rad), $\exp(i\Delta\psi)\approx 1 + i\Delta\psi$, and if the phase mismatch $|\delta|$ of the middle parallel waveguide coupler is also small so $\beta_0 \approx \kappa$ (Eq. (10)), we obtain for small $|\phi_{11}|$ and $|\phi_{22}|$ (<0.5)

$$\phi_{11} \approx \Delta\beta(L+2z_p) + 2\Delta\psi \sin(\beta_0 z_a)\frac{\sin(\beta_0(L+z_a))}{\cos(\beta_0(L+2z_a))} + \delta L\left(\frac{\sin(\beta_0 L)}{\beta_0 L\cos(\beta_0(L+2z_a))} - 1\right) \quad (21)$$

$$\phi_{22} \approx \Delta\beta(L+2z_p) - 2\Delta\psi \sin(\beta_0 z_a)\frac{\sin(\beta_0(L+z_a))}{\cos(\beta_0(L+2z_a))} - \delta L\left(\frac{\sin(\beta_0 L)}{\beta_0 L\cos(\beta_0(L+2z_a))} - 1\right) \quad (22)$$

Comparing with Eqs. (19) and (20), an additional phase term which is proportional to the phase mismatch δ of the middle parallel waveguide coupler appears in the phase responses ϕ_{11} and ϕ_{22} in Eqs. (21) and (22). Figure 6 shows the simulation and modeling results for the coupler CB by fixing the upper waveguide width w_1 at 400nm and changing the lower waveguide width w_2, with other simulation parameters listed in Fig. 6(a) and modeling results provided in Table 1. When w_2 = 410 nm, $\Delta\psi$ is smaller (–0.285, see Table 1) than that in the w_2 = 400 nm case (–0.261), and δ is also negative. As a result, ϕ_{11} first slightly increases with L and then quickly decreases with L, as shown in Fig. 6(b). When w_2 = 390 nm, $\Delta\psi$ is larger (–0.22, see Table 1) than that in the w_2 = 400 nm case (–0.261), and more importantly, δ is positive. From Fig. 6(b) we can deduce that the magnitude of the third term in Eq. (21) is larger than that of the second term, so ϕ_{11} keeps increasing with L instead of changing direction as the case of w_2 = 400 nm. The behavior of ϕ_{22} for different w_2 shown in Fig. 6(c) can be analyzed in a similar way and will not be discussed here.

#118220 - $15.00 USD Received 6 Oct 2009; revised 29 Nov 2009; accepted 30 Nov 2009; published 7 Dec 2009

(a)

coupler	CB
$n_{WG}/n_{Cladding}$	2.829/1
w_1/w_2 (nm)	400/vary
gap (nm)	100
wavelength (nm)	1578

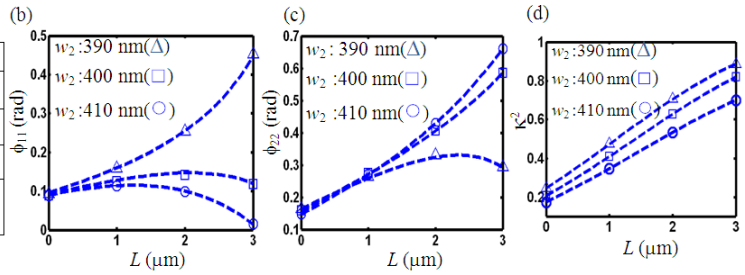

Fig. 6. (a) Simulation parameters for the coupler CB shown in Fig. 1(b). The bend radius R is 6 μm; the *gap* is 100 nm; the upper waveguide width w_1 is fixed at 400 nm, and the simulations are performed for three different values of the lower waveguide width w_2: 390 nm, 400 nm, and 410 nm. Simulation (marker) and modeling (dashed line) results of the coupler CB as a function of the straight part length L are plotted in (b), (c) and (d): (b) phase response ϕ_{11}, (c) phase response ϕ_{22}, and (d) power coupling coefficient κ^2.

3.5 A special case: L = 0 μm

When L = 0 μm, the resonators shown in Fig. 1 will be reduced to the circular structure, and the phase responses of the resulting coupler can be obtained from Eqs. (21) and (22) by setting L = 0 μm:

$$\phi_{11} \approx 2\Delta\beta z_p + 2\Delta\psi \frac{\sin^2(\beta_0 z_a)}{\cos(2\beta_0 z_a)} \tag{23}$$

$$\phi_{22} \approx 2\Delta\beta z_p - 2\Delta\psi \frac{\sin^2(\beta_0 z_a)}{\cos(2\beta_0 z_a)} \tag{24}$$

$$\kappa^2 = \sin^2(2\beta_0 z_a)\cos^2(\Delta\psi) \tag{25}$$

where $\{\beta_0, \Delta\beta\}$ correspond to the coupling parameters of a parallel waveguide coupler with the specified gap, though in the L = 0 μm case the middle straight part does not exist. In fact, by inserting such an interferometric structure (i.e., the parallel waveguide coupler), we are able to extract the unknowns $\{\Delta\psi, z_p, z_a\}$ for the input and output bends, as in the previous examples shown in Figs. 2, 3 and 6. Equations (23) and (24) show that even for the L = 0 μm case, the phase responses ϕ_{11} and ϕ_{22} still have two terms. The first one is proportional to $\Delta\beta$ ($\Delta\beta \equiv (\beta_s + \beta_{as} - \beta_1 - \beta_2)/2$), which has been shown by Eqs. (12) and (13) to be a second-order coupling parameter and will not appear in the first-order CMT. Thus, $\Delta\beta$ has to be determined numerically based on its definition, and can be either positive or negative depending on the specific material systems, in which the sign and magnitude of $\Delta\beta$ can vary dramatically [19].

The second term in Eqs. (23) and (24), which is responsible for the difference between ϕ_{11} and ϕ_{22}, is proportional to $\Delta\psi$. Contrary to $\Delta\beta$ whose property is difficult to predict without specific numerical calculations, $\Delta\psi$ is mainly determined by the geometric properties of the input bend (the bend radius R, the waveguide widths w_1, w_2, and the gap), and its sign and magnitude are in principle predictable, as we have shown for the coupler CB in Fig. 5(b) (a quantitative model for estimating $\Delta\psi$ is out of scope of this paper and will be provided elsewhere). Figure 7(b) plots ϕ_{11} and ϕ_{22} for the coupler CB by fixing w_1 and changing w_2 in the L = 0 case. When w_2 is reduced from a value larger than w_1, $\Delta\psi$ increases from a negative value to an eventual positive value, reflected by the fact that when w_2> 360 nm, ϕ_{22}>ϕ_{11}, and when w_2<360 nm, ϕ_{22}<ϕ_{11}. This is exactly expected from Fig. 5(b). In Fig. 7(b), both ϕ_{11} and ϕ_{22} are positive, indicating a negative CIFS. However, in the material systems that $|\Delta\beta|$ is small, the second term in Eqs. (23) and (24) may dominate. As a result, ϕ_{11} and ϕ_{22} will be of opposite signs, which explains the possibility to observe opposite CIFS in two coupled

#118220 - $15.00 USD Received 6 Oct 2009; revised 29 Nov 2009; accepted 30 Nov 2009; published 7 Dec 2009

microrings with different radii (which is necessary to ensure that $\Delta\psi$ is nonzero), an interesting feature mentioned in the beginning of this paper [9,19].

$\Delta\psi$ also affects the power coupling coefficient κ^2 as shown in Eq. (25), and we notice that the maximum power transfer will be less than 100% if $\Delta\psi \neq 0$, a characteristic feature in a phase mismatched coupler. Thus, we conclude that $\Delta\psi$ is a measure of the phase mismatch of the input bend. Figure 7(c) plots the power coupling coefficient κ^2 for the coupler CB by fixing w_1 and changing w_2 in the L = 0 case. When w_2 reduces, the field overlap between the upper and the lower arms increases. On the other hand, the phase mismatch condition varies more dramatically as w_2 changes and thus is a more decisive factor (the phase mismatch not only affects $\Delta\psi$ but also z_a in Eq. (25)). The maximum power transfer will occur when the upper and the lower arms are close to be phase matched, i.e., $\Delta\psi \approx 0$, which has been confirmed by Fig. 7(c) and also Ref [20], where a detailed discussion of the impact of phase mismatch on the power coupling coefficient κ^2 is presented.

(a)

coupler	CB L=0 μm
$n_{WG}/n_{Cladding}$	2.829/1
w_1/w_2 (nm)	400/vary
gap (nm)	100
wavelength (nm)	1578

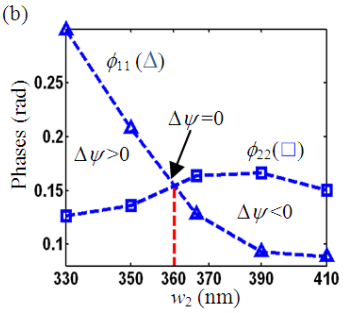

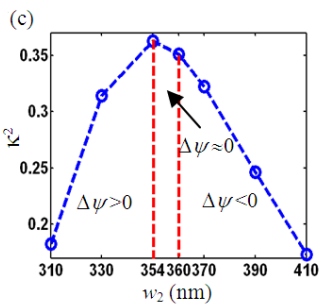

Fig. 7. (a) Simulation parameters for the coupler CB shown in Fig. 1(b) with L = 0. The bend radius R is 6 μm; the *gap* is 100 nm; the upper waveguide width w_1 is fixed to be 400 nm, and the lower waveguide width w_2 varies. Simulation results as a function of w_2 are plotted in (b), (c): (b) phase responses ϕ_{11} and ϕ_{22} (the red dotted line denotes the waveguide width that $\Delta\psi$ = 0), and (c) power coupling coefficient κ^2 (the two red dotted lines denote the waveguide widths corresponding to maximum power transfer and $\Delta\psi$ = 0, respectively).

4. Conclusion

We have shown that for microring resonators, the phase responses of the coupling region of the resonator coupling structure and therefore the CIFS of the corresponding resonators can be quantitatively analyzed by incorporation of the second-order coupling effect and also the geometric effects contributed by the input and output bent parts. The second-order coupling parameter $\Delta\beta$ could be either positive or negative, depending on specific material systems and coupling structures. The geometric parameter $\Delta\psi$, on the other hand, is deterministic and is a measure of the phase mismatch of the input and output bends. With the help of the developed model, qualitative and in some cases quantitative analysis of CIFS for practical 3-D resonator coupling structures without full numerical simulations become feasible. As a particular example, for coupling scheme such as the CA coupler shown in Fig. 1(a), only the second-order coupling effect is present, and CIFS can be easily obtained by calculation of $\Delta\beta$ for a 3-D parallel waveguide coupler with the specified gap, whose calculation only involves an essential 2-D simulation [11]. We believe with the ongoing efforts on quantitative modeling of the geometric parameter $\Delta\psi$, a fast and efficient estimation of CIFS for common coupling structures such as the CB coupler shown in Fig. 1(b) is possible in the near future.

Acknowledgments

This work was supported by Air Force Office of Scientific Research under Contract No. FA9550-06-01-2003 (G. Pomrenke). The authors are also grateful to A. Eftekhar for helpful discussions.

#118220 - $15.00 USD Received 6 Oct 2009; revised 29 Nov 2009; accepted 30 Nov 2009; published 7 Dec 2009

Appendix A. Simulation details and CIFS calculation

The simulations in this paper are performed with an in-house FEM code by implementing the 2-D Helmholtz equation in the Comsol environment. More than 200,000 cubic elements with grid sizes less than 20 nm are used to resolve the structure.

This paper has assumed that the CIFS calculation is equivalent to the calculation of the phase responses of the coupling region through the connection established by Eq. (2). We will provide an example here to verify this equivalence, which is critical since the most of discussions of CIFS in this paper are based on the phase responses of the coupling region. Figure 8(a) shows the simulated structure, which is a microring side coupled to a straight waveguide. By solving the eigenvalue problem of the system, the resonance frequency of the resonator is obtained [21]. According to its definition, CIFS is the difference of the resonance frequencies of the same mode with and without the coupled waveguide. Figure 8(c) compares the simulation results of CIFS via this eigenvalue solution to the phase response method by simulating the coupler CB at L=0 case and converting the phase results to CIFS through Eq. (2) for different gaps. Good agreement is obtained, and our assumption that the phase response study is equivalent to the direct CIFS study is justified.

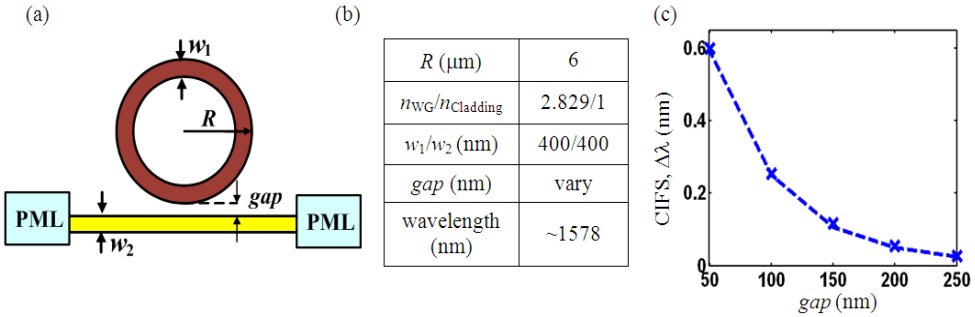

Fig. 8. (a) Structure used for CIFS simulation using a complex-frequency eigenmode solver: a microring with an outer radius R coupled to a straight waveguide. The brown region is the waveguide core with refractive index n_{WG}, and the yellow region can be either waveguide core or cladding to obtain the coupling effect on the resonance frequency shift of the resonator. (b) Simulation parameters for the structure shown in (a). (c) CIFS obtained via the eigenvalue solution (dashed line) and the phase response method (cross), respectively (note that CIFS is shown in shift in wavelength, and a positive shift in wavelength means a negative CIFS).

Appendix B. Calculation of normalization matrix *N*

Strictly speaking, when the coupling is negligible (for example, by increasing the gap to a large enough value so that β_0~0, $\Delta\beta$~0) the free propagation phases are not necessarily $\exp(i(\alpha_0+\Delta\psi))$ for the upper arm, and $\exp(i(\alpha_0-\Delta\psi))$ for the lower arm for the fixed reference planes of $[a_1, a_2]^T$ and $[c_1, c_2]^T$. Suppose $\Delta\psi$ needs to be replaced by $\Delta\psi'$ in Eq. (15) for the normalization matrix N, then Eqs. (19) and (20) become,

$$\phi_{11} \approx \Delta\beta(L+2z_p) + 2\Delta\psi \sin(\beta_0 z_a)\frac{\sin(\beta_0(L+z_a))}{\cos(\beta_0(L+2z_a))} + 2(\Delta\psi - \Delta\psi') \qquad (26)$$

$$\phi_{22} \approx \Delta\beta(L+2z_p) - 2\Delta\psi \sin(\beta_0 z_a)\frac{\sin(\beta_0(L+z_a))}{\cos(\beta_0(L+2z_a))} - 2(\Delta\psi - \Delta\psi') \qquad (27)$$

From Eqs. (26) and (27) we see that there will be a constant proportional to $(\Delta\psi-\Delta\psi')$ (a factor of 2) added to ϕ_{11}, and the same constant subtracted from ϕ_{22}. Clearly when the gap is large, $\Delta\psi-\Delta\psi'$ is negligible. We can estimate the effect of the coupling on $\Delta\psi-\Delta\psi'$ by reducing the gap to the specified number from a general asymmetric parallel waveguide coupler, whose transfer matrix is given by Eq. (9). Note that the reference planes for the

#118220 - $15.00 USD Received 6 Oct 2009; revised 29 Nov 2009; accepted 30 Nov 2009; published 7 Dec 2009

parallel waveguide coupler are chosen such that the off-diagonal elements are equal in Eq. (9) (that's the reason we make the same choice of reference planes for the input bend in Eq. (14)). A simple calculation shows that

$$(\Delta\psi - \Delta\psi') \approx \delta L(\frac{\tan(\beta_0 L)}{\beta_0 L} - 1) \tag{28}$$

For the input bend, the effective length L is approximately z_a, and $\tan(\beta_0 L) \approx \beta_0 L + (\beta_0 L)^3/3$. Thus, we can simplify Eq. (28) to be

$$(\Delta\psi - \Delta\psi') \approx \delta z_a (\beta_0 z_a)^2 / 3 \tag{29}$$

For the examples shown in Table 1, by substituting the corresponding values to Eq. (29) this amount can be calculated to be very small (<0.002 rad) and thus is negligible (the fitting error is on the order of 0.005 rad).

When the phase mismatch parameter $|\delta \equiv (\beta_1 - \beta_2)/2|$ is very large so that $|\delta| \sim \kappa$, $\Delta\psi - \Delta\psi'$ can be comparable to other terms in Eqs. (26) and (27), and the presented model will have appreciable errors. However, in this case, expansion of the individual waveguide modes to the lowest two system modes usually is not sufficient, and the expansion basis has to be enlarged in Eq. (9). These complex situations are out of scope of this paper and will not be discussed.

#118220 - $15.00 USD Received 6 Oct 2009; revised 29 Nov 2009; accepted 30 Nov 2009; published 7 Dec 2009